



## Research articles

## Automated meshing of electron backscatter diffraction data and application to finite element micromagnetics



Markus Gusenbauer<sup>a,\*</sup>, Johann Fischbacher<sup>a</sup>, Alexander Kovacs<sup>a</sup>, Harald Oezelt<sup>a</sup>, Simon Bance<sup>b</sup>, Panpan Zhao<sup>c</sup>, Thomas George Woodcock<sup>c</sup>, Thomas Schrefl<sup>a</sup>

<sup>a</sup> Department for Integrated Sensor Systems, Danube University Krems, Austria

<sup>b</sup> Seagate Technology, Derry, Northern Ireland, United Kingdom

<sup>c</sup> IFW Dresden, Institute for Metallic Materials, Germany

## ARTICLE INFO

## Keywords:

Micromagnetic simulations  
EBSD  
Adaptive finite element mesh  
MnAl  
Domain wall pinning  
Gilbert damping constant

## ABSTRACT

This paper gives a procedure for automatically generating finite element meshes with an adaptive mesh size from Electron Backscatter Diffraction (EBSD) data. After describing the procedure in detail, including preliminary and image processing steps, an example application is given. The method was used to carry out finite element (FE) micromagnetic simulations based on real microstructures in the hard magnetic material, MnAl. A fast micromagnetic solver was used to compute hysteresis properties from the finite element mesh generated automatically from EBSD data. The visualization of the magnetization evolution showed that the reversal is governed by domain wall pinning at twin boundaries. The calculated coercive fields are very sensitive to changes of the Gilbert damping constant, even for low field rates.

## 1. Introduction

The magnetic properties of MnAl-C permanent magnets are strongly affected by the presence of defects in the microstructure which can act as nucleation or pinning sites for magnetic domain walls [1–6]. A one-dimensional model has been established by Zijlstra to calculate the nucleation and pinning fields at antiphase boundaries in MnAl magnets [1] but other types of defects, e.g. twin boundaries remain less well understood. Electron backscatter diffraction (EBSD) has been used to analyse the type and spatial distribution of twin boundaries in such materials [7]. However, a full understanding of the effect of defects on the magnetic properties can only be obtained by combining this data with results from finite element (FE) micromagnetic simulations.

FE models are often based on artificially generated microstructures using e.g. the random polycrystalline generator NEPER [8]. In one study, this approach has been used to analyse the magnetic properties and chemical composition of rare earth permanent magnets [9]. The accuracy of FE models based on simulated microstructures is limited as they often represent only an approximation to the real microstructure. Recent advances in numerical methods [10], computing power, and structural characterization have led to FE micromagnetic simulations of permanent magnets that take into account microstructural features in greater detail [11,12] but producing FE models which are directly

based on real microstructures remains highly desirable.

The direct production of FE models from EBSD data of real microstructures in MnAl-C has recently been demonstrated [2] and other materials have also been analysed in this way e.g. [13]. Computer aided design methods have been used to reconstruct polycrystalline metals [14]. In biomedical research there is a great interest of converting real patient images (e.g. from magnetic resonance imaging, ultrasound) to computer models [15]. In order to solve homogenization problems in imaging data the Level Set Method has been applied by Legrain and co-workers [16]. Due to the high need in the automotive industry to analyze the mechanical stability of metals a digital material representation technique has been used [17]. They split the conversion problem based on imaging data of a dual phase steel into microstructure regeneration, application of material parameters, meshing of the microstructure and computational modeling. Just recently the mechanical deformation of Duplex stainless steels have been investigated based on a close to automatic environment for meshing complex microstructures [18].

The procedure to create the FE models contains several independent steps and the aim of the current work is to develop an automated meshing routine which yields high quality finite element meshes from EBSD data. The new workflow is based on existing open-source software packages and self-written computer code. The technique

\* Corresponding author.

E-mail address: [markus.gusenbauer@donau-uni.ac.at](mailto:markus.gusenbauer@donau-uni.ac.at) (M. Gusenbauer).

<https://doi.org/10.1016/j.jmmm.2019.165256>

Received 11 February 2019; Received in revised form 30 April 2019; Accepted 30 April 2019

Available online 02 May 2019

0304-8853/ © 2019 The Authors. Published by Elsevier B.V. This is an open access article under the CC BY license (<http://creativecommons.org/licenses/by-nc-nd/4.0/>).

developed will be applied here to generate FE models for micro-magnetic simulations of twin boundaries in MnAl-C permanent magnets, but it is applicable to any material. The analyzed composition  $\text{Mn}_{53}\text{Al}_{45}\text{C}_2$  (at.%) is an as-transformed sample without an overall preferred orientation of the grains as described by Bittner and co-workers [7]. Owing to the change of easy directions across twin boundaries we expect domain wall pinning at those interfaces. Basic micromagnetic simulations show that domain walls move towards domain walls of a misoriented grain, where they remain pinned due to a reduced exchange and anisotropy energy [19].

We use the generated structures in order to demonstrate the influence of magnetization dynamics on the coercivity of MnAl-C permanent magnets. Our computational results show that the magnetization curves computed by following the path given by the solution of the Landau-Lifshitz-Gilbert (LLG) equation give lower switching fields than computations that do not include magnetization dynamics, such as energy minimization. Similar results were reported by Leineweber and Kronmüller, who showed that the nucleation field for small NdFeB magnetic particles depends on the rate of change of the external field [20,21]. Due to fast changes in the energy landscape the system does not reach the nearest metastable state. Thus reversed magnetic states may be found at external fields which are up to 20 % smaller than the ideal nucleation field. Here we show that the pinning field of domain walls at twin boundaries depend on magnetization dynamics also for low field rates.

### 1.1. Content of the paper

The work is split into the Methods and Theory section and the Results section. Firstly the transfer from EBSD MnAl-C data to a finite element mesh is explained in detail. Data conversion is necessary to obtain a pixelated bitmap image, as well as a precise and careful image manipulation. The actual meshing procedure is a two-step process and explained later on. The micromagnetic solver is briefly described as well. In the Results section the needed finite element size is calibrated with an idealized cuboidal two-grain model. A reduction of original data complexity reduces the computational demand, therefore we are merging similar crystallographic orientations according to the results in Section 3.2. Lastly some selections of the EBSD data are exemplarily meshed and computed, and discussed later on.

## 2. Methods and theory

In the methods section all the steps necessary to get the EBSD data to the final micromagnetic simulation are explained. The pathway and used software tools are the authors' choices (Fig. 1). The steps necessary to create a finite element mesh from the EBSD data can be done using the graphical user interface (GUI) of the respective software tools as indicated by the pathway labeled with G. Alternatively, the steps can be automated by the use of the Python programming language (Python Software Foundation, [www.python.org](http://www.python.org), version 2.7, last visited on April 10, 2018) and the command line interface of the software tools (labeled with A). The most important commands are listed in Algorithm 1. For easy reproduction in other fields of research open-source

software is preferred. Several other pathways to the solution are possible. The required computation steps are called consecutively via subprocesses, and checked afterwards for completeness. Temporary files transfer necessary information to the next subprocess in the list.

#### Algorithm 1 Python master script (basic steps as pseudo code)

- (a) [dream3d.bluequartz.net](http://dream3d.bluequartz.net), last visited on April 10, 2018
- (b) [github.com/migvel/color\\_trace](https://github.com/migvel/color_trace), last visited on April 9, 2018
- (c) [inkscape.org](http://inkscape.org), last visited on April 9, 2018
- (d) Python Imaging Library (PIL), [www.pythonware.com/products/pil](http://www.pythonware.com/products/pil), last visited on June 6, 2018
- (e) Iso2Mesh [22]

**Require:** EBSD dataset in Oxford Instruments format (*data.ctf*)

1: *PipelineRunner -p pipeline.json*

▷ (a) *pipeline.json* created once in DREAM.3D GUI to convert orientations (*data.ctf*) to inverse pole figure (IPF) colors (*data.png*).

**Require:** Store grain orientations for the micromagnetic solver.

**Ensure:** Bitmap image of IPF colors (*data.png*) is created.

2: *python color\_trace.py < input folder > -colors < N > < output folder >*

▷ (b) Vectorization of bitmap image and smoothing boundaries

**Ensure:** Smoothed boundaries vector image (*smoothed\_data.svg*) is created.

3: *inkscape -z -e upscaled\_smoothed\_data.png -w < width > -h*

*< height > smoothed\_data.svg*

▷ (c) Upscaling of smoothed boundaries

**Ensure:** Upscaled bitmap image (*upscaled\_smoothed\_data.png*) is created.

▷ (d) Pixelwise manipulation of *upscaled\_smoothed\_data.png* (Cropping, handle grain boundaries)

▷ Create *data.txt* file with pixelwise replacement of color information to unique grain id (from 0 to 255)

**Ensure:** Enhanced bitmap with unique grain ids (*data.txt*) is created.

4: *meshing.m*

▷ (e) Matlab/octave script to convert *data.txt* to uint8, applying vol2mesh using cgalmesh and exporting the mesh

**Ensure:** Mesh file is created and correct grain orientations are available.

▷ Apply micromagnetic solver using mesh file and grain orientations.

### 2.1. Data conversion

The data of the microstructure of MnAl-C are acquired using a field emission gun (FEG) scanning electron microscope (SEM) in combination with electron backscattered diffraction (EBSD). The data contains a set of crystallographic orientation information of the scanned material. The orientation information is stored as Euler angles, which can be transformed to orientation matrices.

DREAM.3D is a convenient software package to reconstruct EBSD data ([dream3d.bluequartz.net](http://dream3d.bluequartz.net), last visited on April 10, 2018), which in our case is stored in an Oxford Instruments (.ctf) format. We read the EBSD input file and convert the orientation information to inverse pole figure (IPF) colors with a [001] reference direction. The resulting image is then exported to a bitmap (.png) format (Fig. 2 on the left).

Another possibility is the readout of EBSD data using our own Python code. The original data points are merged into regions with similar orientations. Each region is given a unique label and the average orientation is computed using the procedure given in [23]. From the labels file again a bitmap image can be created using the Python Imaging Library (PIL, [www.pythonware.com/products/pil/](http://www.pythonware.com/products/pil/), last visited on June 6, 2018).

It is important to consider the region of interest in the orientation

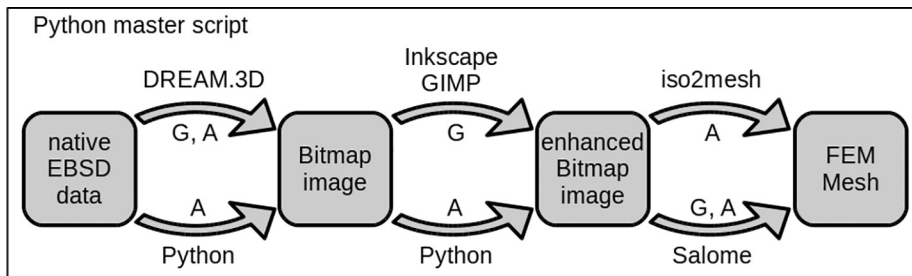


**Fig. 1.** Software tools are shown for finite element meshing of native EBSD data with intermediate image manipulation for enhancing the quality of the image. G refers to the use of the graphical user interface (GUI, manual data handling), whereas A denotes automated processes. Some tools have a GUI to create an automation script (G,A). The pseudo code for the automated toolchain is shown in Algorithm 1.

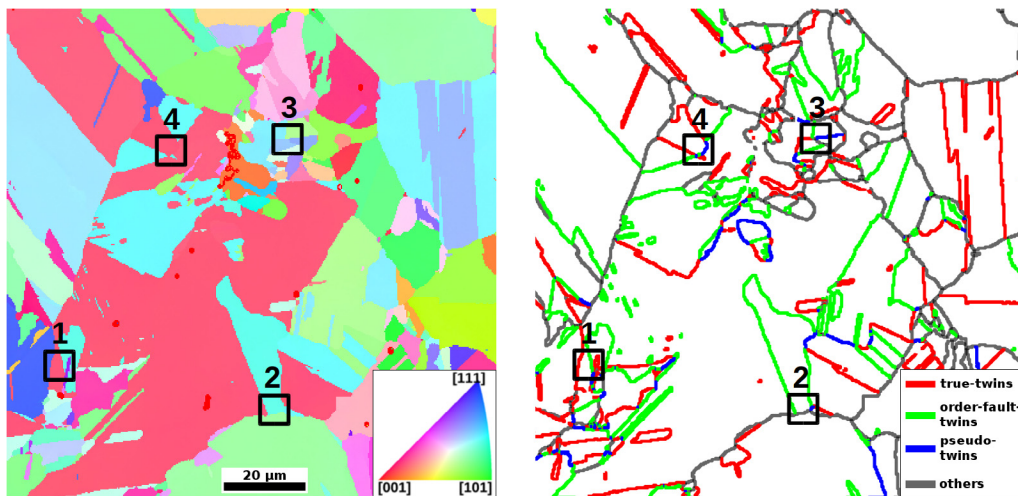


**Fig. 2.** Inverse pole figure (IPF) map of an as-transformed MnAl-C microscopic EBSD slice ( $120\mu\text{m} \times 120\mu\text{m}$ , with a resolution of  $0.3\mu\text{m}$  per datapoint) converted with Dream3D (dream3d-bluequartz.net, last visited on April 10, 2018) on the left. Crystallographic twin boundaries on the right: true-twins (red), order-fault-twins (green), pseudo-twins (blue) and other boundaries (gray) with a misorientation angle of about  $180^\circ$ ,  $118^\circ$ ,  $62^\circ$  and various other angles respectively. The black squares indicate the selections for the finite element simulations in the results section. (For interpretation of the references to colour in this figure legend, the reader is referred to the web version of this article.)

dataset, especially with respect to the limitation of computer power. If only certain regions are relevant, or the computer memory is limited during meshing, the data has to be cut before running the automated meshing procedure. This can be done either directly in DREAM.3D, using coordinate information with the Python language or with an image manipulation tool (e.g. GIMP, [www.gimp.org](http://www.gimp.org), last visited on April 10, 2018). A graphical user interface is necessary to initially interpret the microscope data and to find the most important regions.

Twin boundaries were identified using the same criteria as described in [7] i.e. if the misorientation axis of the two grains forming the boundary is within  $2^\circ$  of the normal to one of the  $\{111\}$  planes and the misorientation angle is  $62^\circ \pm 2^\circ$ ,  $118^\circ \pm 2^\circ$  or  $180^\circ \pm 2^\circ$ , the boundary can be described as a pseudo-twin, order-twin or true-twin, respectively. A bitmap containing the locations of the general grain boundaries and the three types of twins can then be plotted (Fig. 2 on the right).

Reducing the complexity of the raw EBSD data is possible by merging similar neighboring crystallographic orientations. In Section 3.2 we compute the pinning and nucleation fields of neighboring orientation areas with increasing angle between their orientation axes. The raw data can be quantified with a step size of a few degrees without losing important information. Here again the Python language is useful to find similar crystallographic orientations. In Fig. 2 neighboring orientation areas with an angle difference of less than 5 degrees are assumed to be a single orientation area.

## 2.2. Image manipulation

EBSD data points are arranged on a regular grid. Features which are small with respect to the grid size are therefore resolved coarsely and their boundaries contain sharp angles (Fig. 3(a)), which can lead to numerical instabilities during the further computations. Using several

image manipulation steps, the rough corners of the orientation areas are smoothed and scaled up to create a high resolution bitmap image (Fig. 3(a–c)). Different colors of the processed image are listed as individual orientations. Here it is not important if the image has inverse pole figure (IPF) colors, Euler RGB coloring or any other color encoding [24]. In the end, after finishing the image manipulation, every pixel group with the same color should have the same orientation, which can be traced back to the original data.

In the first step of image manipulation the bitmap image is converted to a vector graphic (Fig. 3(b)). Here the corners of the multi colored image are smoothed using the color trace algorithm found at [github.com/migvel/color\\_trace](https://github.com/migvel/color_trace), last visited on April 9, 2018. It makes use of the potrace (a polygon-based tracing) algorithm (potrace.sourceforge.net, last visited on April 9, 2018), which is meant for black and white image vectorization. The algorithm basically splits the image according to its color, converts it to black and white, performs the potrace vectorization algorithm and merges the resulting files. The potrace algorithm is critical close to the images boundary. Here resulting shapes diverge from the original (Fig. 3(b)). Therefore it is beneficial to cut a certain frame from the bitmap image (Fig. 3(c)). In order not to lose important information the initial bitmap image should be chosen large enough.

The resulting vector graphic is scaled up and converted back to a bitmap image, which is necessary later on for meshing. Due to the color trace algorithm (merging of individual color vectorizations), the boundaries of the orientation areas sometimes do not precisely overlap. We are using a self written Python code to detect and remove those boundaries. Converting a vector graphic to a bitmap image creates some intermediate gradient colors between 2 neighboring orientation areas (Fig. 4(a)). The Python algorithm counts the amount of data points per color. Under a certain threshold, the boundary colors can be detected and removed (Fig. 4(b)). Filling up the empty holes is

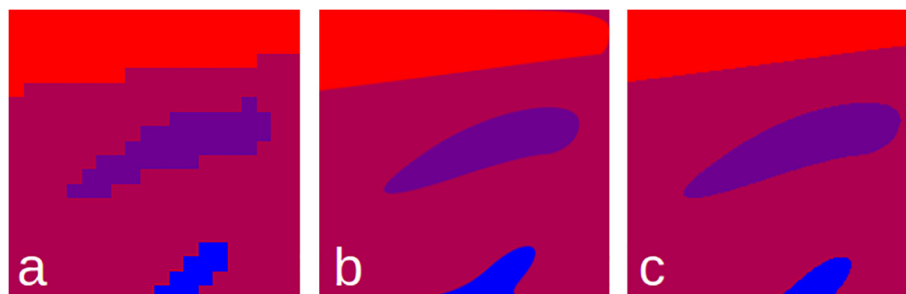


**Fig. 3.** Image manipulation from a highly pixelated bitmap image (a) to a vectorized image (b) and a high resolution smoothed bitmap image with a cut of a certain inaccurate pixel frame (c).

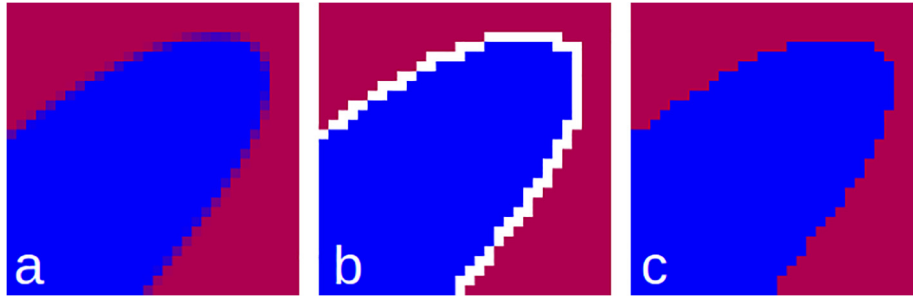


Fig. 4. Intermediate gradient colors between orientation islands (a) are firstly removed (b) and later on filled with a simple game of life algorithm (c).

performed with a simple game of life algorithm. Each empty (white) pixel gets the pixel information of the most present neighbor (Fig. 4(c)). The boundaries of the objects in the final bitmap image necessarily contain sharp angles; however, these are on a far smaller scale than those in the original data and therefore have a much smaller effect on later computations. All image processing steps within the Python framework are performed with the help of the Python Imaging Library.

### 2.3. Meshing

For micromagnetic simulations we require a 3-dimensional tetrahedral mesh of the material composition. As the experimental EBSD data in this work are 2-dimensional, a mesh with slab geometry in 3D is generated by stacking several copies of the 2D meshed experimental data. In later works, it is planned to fill the stack with sequential layers of EBSD data rather than copies of one layer. In this way true 3D microstructure data will be available for meshing. Iso2mesh, a matlab/octave based toolbox, is highly capable of converting bitmap information into tetrahedral meshes [22]. Using the Computational Geometry Algorithms Library (CGAL) [25], uint8 data (unsigned 8-bit integer: numbers from 0 to 255 according to the color/orientation) is firstly converted to isosurfaces (islands of the same number). Using Iso2mesh we extrude the crystallographic pattern to a thin magnetic film and generate a volumetric finite element mesh. Such a model of the sample may be used in the future to simulate domain wall processes observed by Lorentz electron microscopy. Parameters for tuning the mesh are the maximum tetrahedral element volume and radius, and the maximum deviation from the isosurfaces. As a result, nodes, elements and faces of the tetrahedral mesh are written into text files and can be converted to a number of desired formats. Various file formats are supported by Iso2mesh itself, whereas other file formats can be generated using Python. A comparison of the final mesh is shown for a pixelated input bitmap image (Fig. 5) and an enhanced bitmap image (Fig. 5(b,c)). In Fig. 5(a) the boundaries are somewhat rounded, but still following the pixelated input data. Whereas in the enhanced meshes, the boundaries are much more smoothed. In Fig. 5(c) the adaptive meshing algorithm of CGAL is shown. We use the ParaView data visualization toolkit [26] to view the generated meshes from Iso2mesh.

One downside of the CGAL algorithm is the poor resolution of contact surfaces between two islands. Those surfaces are mostly uneven

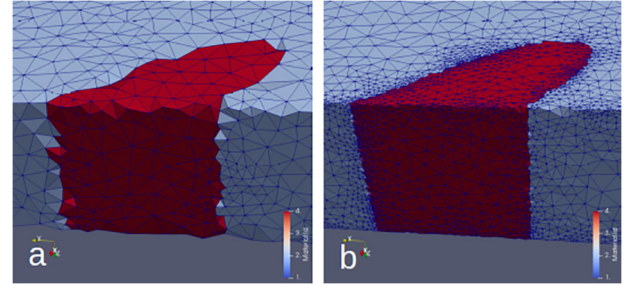


Fig. 6. Comparison of coarse mesh problems at boundaries (a) and coarse mesh with increased resolution of the boundaries (b). An adaptive mesh size is applied, when reducing the deviation to the isosurface parameter.

and comprise hills and valleys. Using a rather small allowed deviation from the isosurface reduces the error, but increases the number of mesh elements tremendously (Fig. 6). The CGAL algorithm uses an adaptive mesh size, which is more dense close to the isosurfaces (depending again on the allowed deviation from the isosurface), which is important to accurately compute the exchange of different orientation areas.

The computational costs are related with the number of finite elements in the simulated system. In Section 3.1 we compute the largest possible mesh size, with no or only little difference in final results.

Computing the magneto-static interaction field using a magnetic scalar potential is an open boundary problem. This can be most easily solved by expanding the computational mesh outside the magnetic region [27], which we refer to as air box. We are using the pre- and post-processing software tool Salome (salome-platform.org, last visited on 16/05/2018) to wrap an adaptive mesh around the initially created mesh from Iso2mesh. This can be done either in the graphical user interface of Salome or in its Python interface. The air box is about 11 times larger than the chosen material sample with a coarse mesh size 10 times the initial mesh size.

### 2.4. Micromagnetic simulations

Computing the magnetic state of a material in an applied external field requires the minimization of the total energy in the system [28]. One way of solving the problem is minimizing the Gibb's free energy,

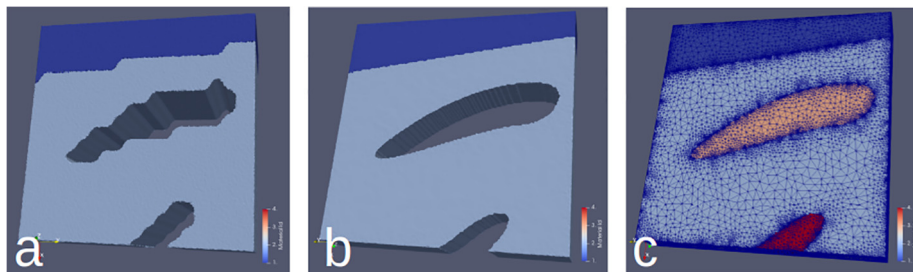


Fig. 5. Tetrahedral mesh from the original bitmap image (a), the enhanced bitmap image (b) and the triangulated surface mesh with adaptive mesh size (c).



**Table 1**

Micromagnetic simulation parameters of the analyzed MnAl-C material. Parameters are obtained from bulk MnAl-C [30]

Parameter	Value	Unit
Temperature T	300	K
magnetic polarization $J_s$	0.8	T
exchange constant A	19.9	pJ/m
uniaxial anisotropy constant K	1.5	MJ/m <sup>3</sup>

which is the sum of exchange energy, anisotropy energy and the energy of the demagnetization field and external field. Another possibility is the description by the magnetic moments in the system using the Landau-Lifshitz-Gilbert (LLG) equation. Here every quantized magnetic moment is precessing around the effective field. Using a damping term the magnetic moment approaches the energetically favorable equilibrium state (parallel to the field). The LLG equation is time dependent whereas minimizing the Gibb's free energy computes static solutions only. Consequently the LLG equation is much more computationally demanding. Both methods require a finite element mesh, representing the magnetic moments of the material, in which the differential equations are solved. The optimal mesh size is computed in Section 3.1 for MnAl-C. In Section 3.4 we are using the time dependent LLG equation to analyze the relationship between twin boundaries and spin waves in the magnetization reversal [29]. In Table 1 we show the micromagnetic simulation parameters.

### 3. Results

In the results section the optimal mesh size for MnAl-C compounds is discussed. Reduction of the microscopic data complexity can be achieved by correcting very small deviations of the angles between two neighboring orientation areas. For this preliminary calibration steps we use a simplified model of two cuboidal MnAl-C grains (Fig. 7) where we compute and analyze nucleation fields  $H_n$  and pinning fields  $H_p$ . The easy axis of the first grain is parallel to the field direction. The easy axis of the second grain is tilted with an angle  $\Theta$  with respect to the first grain. With this simplified model a two-domain state in the energy minimum, caused by the magnetostatic energy, would hinder domain wall motion. Since we want to investigate pinning fields in the numerical tests with the two-grain model, we do not take into account the magnetostatic energy.

Later on, magnetic reversal curves are computed and discussed for specific areas of the microscopic data to obtain a deeper insight into the MnAl-C magnetic behavior.

#### 3.1. Finite element mesh size

The mesh size is basically the value for the largest edge length of the

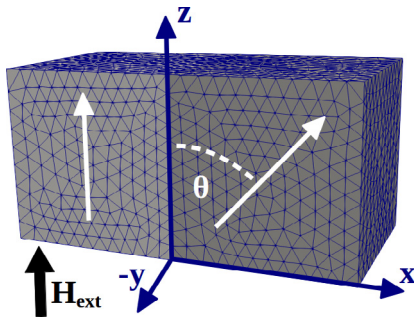


**Fig. 7.** Finite element model for mesh size and angular dependency calibration. The edge length of the two MnAl-C cubes is 60 nm. The crystallographic orientations (easy axes) of the two grains are parallel and tilted by an angle  $\Theta$  with respect to the z-axis, respectively.

tetrahedral finite element. It should be related to the characteristic length scales of the material; the Bloch parameter

$$\delta_0 = \sqrt{A/K}, \quad (1)$$

and the exchange length

$$l_{ex} = \sqrt{2\mu_0 A/J_s^2} \quad (2)$$

These lengths are related to the change of magnetization within a Bloch or a Néel wall. The Bloch wall width and the Néel wall width are given by  $\pi\delta_0$  and  $\pi l_{ex}$ , respectively. In order to resolve the transition of the magnetization between two domains, the mesh size has to be smaller than the smallest characteristic length of the material. For MnAl we obtain  $\min(\delta_0, l_{ex}) = 3.6$  nm.

In Fig. 8 on the left we show the nucleation fields  $H_n$  and the pinning fields  $H_p$  of the simplified two-grain model (Fig. 7) as a function of mesh size. To compute  $H_n$ , both grains are initially saturated in z-direction and then reversed by an external field ( $\mu_0 H_{ext}$  from +2 T to -4 T) in 40 mT/ns. For the computation of  $H_p$  we start with an initial configuration  $M_z/M_s = -1$  for the left grain and  $M_z/M_s = 1$  for the right one. Here the field  $\mu_0 H_{ext}$  is changed by the same rate from 0 T to -2 T.

There is only a marginal change in  $H_n$  with respect to the mesh size, whereas the computation of  $H_p$  requires mesh sizes less than 5 nm to show acceptable deviations. For the rest of the study we choose a mesh size of 3 nm. The number of finite elements increase drastically below 3 nm (Fig. 8 on the left, 2nd y axis). The EBSD data analyzed in this work is on the microscale, which requires a certain scaling for computational investigation (see Section 3.3).

#### 3.2. Reduction of EBSD data complexity

To incorporate the magnetocrystalline easy axes in the FE model, the regions of homogeneous orientation have to be defined. When the EBSD data is processed, very small changes in orientation will prompt a new region which results in a very complex structure. To reduce the number of such regions and hence also the required computing resources, the tolerance for the change in orientation can be increased, i.e. we can merge neighboring regions with small orientation differences. To do this, we first have to determine the maximum deviation angle possible without changing the simulation results. We use the two-grain model with 3 nm mesh size and compute the reversal again for various angles  $\theta$ . The resulting  $H_n$  and  $H_p$  are plotted against  $\theta$  in Fig. 8.

The response of the nucleation field  $H_n$  with increasing angle  $\Theta$  is much higher than with the pinning field  $H_p$ . The change of nucleation field  $H_n$  with increasing angle  $\Theta$  resembles the Stoner Wohlfahrts curve for ideal magnets [31]. In further simulations we are especially interested in pinning effects at twin boundaries. We choose a tolerance angle of 5° to merge neighboring regions (see Fig. 2) which corresponds to a maximal change of 68 mT of the pinning field.

#### 3.3. Micromagnetic models of crystallographic defects

The computation of magnetization reversal curves for the models created from the EBSD data requires a certain scaling. Using the magnetic properties of MnAl-C (Table 1) a mesh size of 3 nm is a good trade-off between accuracy and demand for computing resources (see Section 3.1). The data set given in Fig. 2 has a length of 120  $\mu\text{m}$  with a pixel length of 0.3  $\mu\text{m}$ . Computing the reversal of the whole slice with a thickness of 1  $\mu\text{m}$  would require more than 3 trillion finite elements, which is currently unrealistic to compute, unless using extensive amount of computer power with a high efficiency in parallelization [9]. Similar to Bance et al. [2] we are downscaling the native EBSD dataset for predicting real size behavior. 1  $\mu\text{m}$  of the original data corresponds to 33 nm in our simulation model. In Fig. 9 we show intermediate states of the automated meshing procedure for specific areas in the native EBSD microscopic slice (see small squares in Fig. 2). The original data

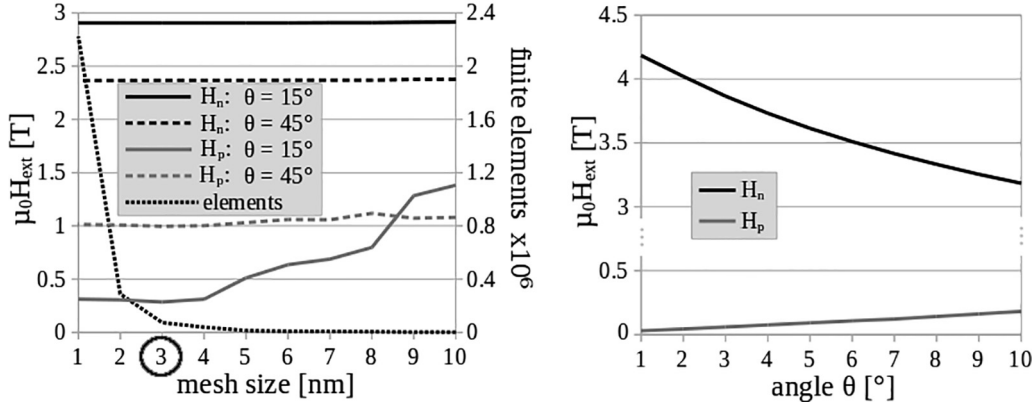


**Fig. 8.** Calibration of the optimal mesh size using nucleation fields  $H_n$  and pinning fields  $H_p$  at an angle  $\Theta$  of  $15^\circ$  and  $45^\circ$  (left). The number of finite elements with respect to the used mesh size is shown on the second y axis on the left. The angular dependency of  $H_n$  and  $H_p$  on  $\Theta$  in the range of  $0^\circ$  and  $10^\circ$  is shown on the right. For angular dependency calculations we use an optimal mesh size of 3 nm. Results are obtained with the finite element model in Fig. 7.

(Fig. 9 col. 1) is automatically improved by the image manipulation steps described in Section 2.2 (Fig. 9 col. 2). Next to the enhanced bitmap image the twin boundaries are visualized (Fig. 9 col. 3). The final upscaled bitmap image is meshed using the Iso2mesh toolbox (Fig. 9 col. 4) and further extended with an airbox for computing the stray field using the Salome software package. (See Fig. 10).

### 3.4. Spin wave dynamics at twin boundaries

We are interested in the switching dynamics close to twin boundaries, therefore we compute a full magnetization reversal curve by solving the LLG equation with an applied external field of 4 T to  $-4$  T (in-plane y direction) changed linearly in a time of 200 ns. This corresponds to a dimensionless field rate  $\beta = 10^{-5}$  as defined by Leineweber

and Kronmüller [21]. They reported differences in static and dynamic calculations only for fastly switching fields (large field rates) and low damping. We change the intrinsic Gilbert damping constant  $\alpha$  to see the influence on the switching behavior. Yilgin et al. investigated  $\text{Co}_2\text{MnAl}$  Heusler alloy films and found damping values of 0.014 to about 0.07 depending on the annealing temperature [32]. The damping is typically measured in thin ferromagnetic films. It can be derived from the line-width of ferromagnetic resonance (FMR) spectra [33]. In micro-magnetic simulations many authors set the damping constant to 1 for numerical convenience. A damping constant of 1 is expected to give the fastest reversal time [20,34]. We compare the numerical results for nucleation and pinning at twin boundaries for a damping constant  $\alpha = 1.0$  and  $\alpha = 0.02$ . We use an initial state uniformly magnetized in +y direction.

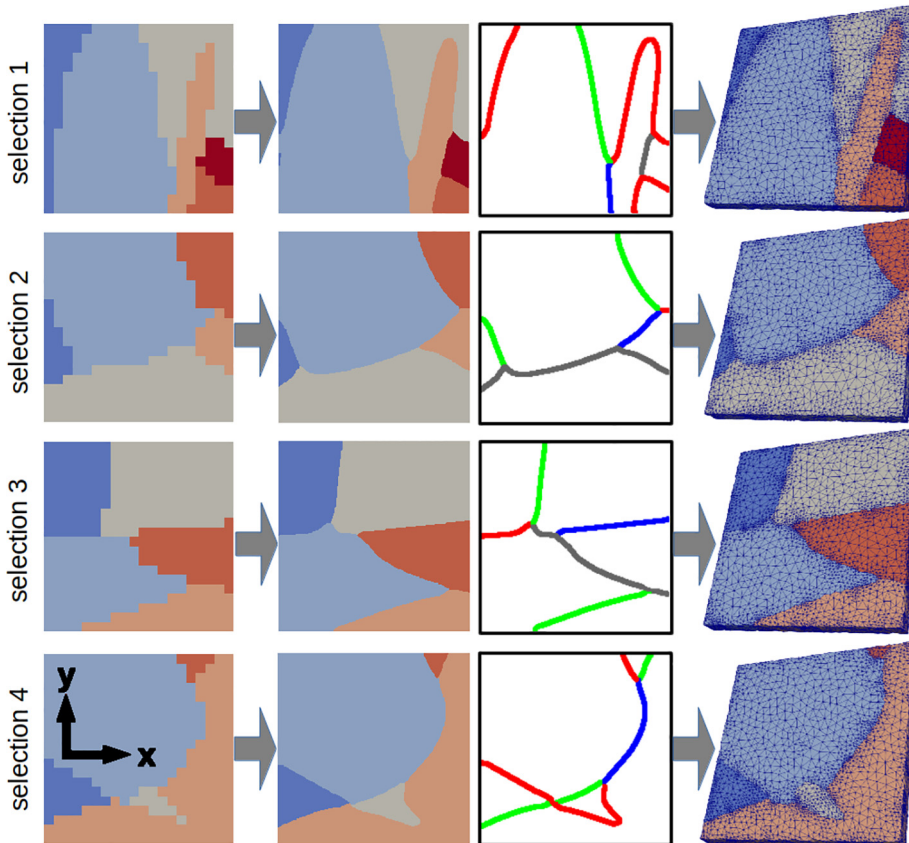


**Fig. 9.** Selections 1 to 4 from the native EBSD data in Fig. 2. The pixelated data (col. 1) is improved through automated vectorization, upscaling and refinement (col. 2) as explained in Section 2.2 and meshed with a downscaling factor of 100 (col. 4) to reduce needed computational resources. Twin boundaries are shown in col. 3: true-twins (red), order-fault-twins (green), pseudo-twins (blue), other boundaries (gray). Colors in the selected images are chosen arbitrary for increased contrast necessary in the image manipulation. (For interpretation of the references to colour in this figure legend, the reader is referred to the web version of this article.)

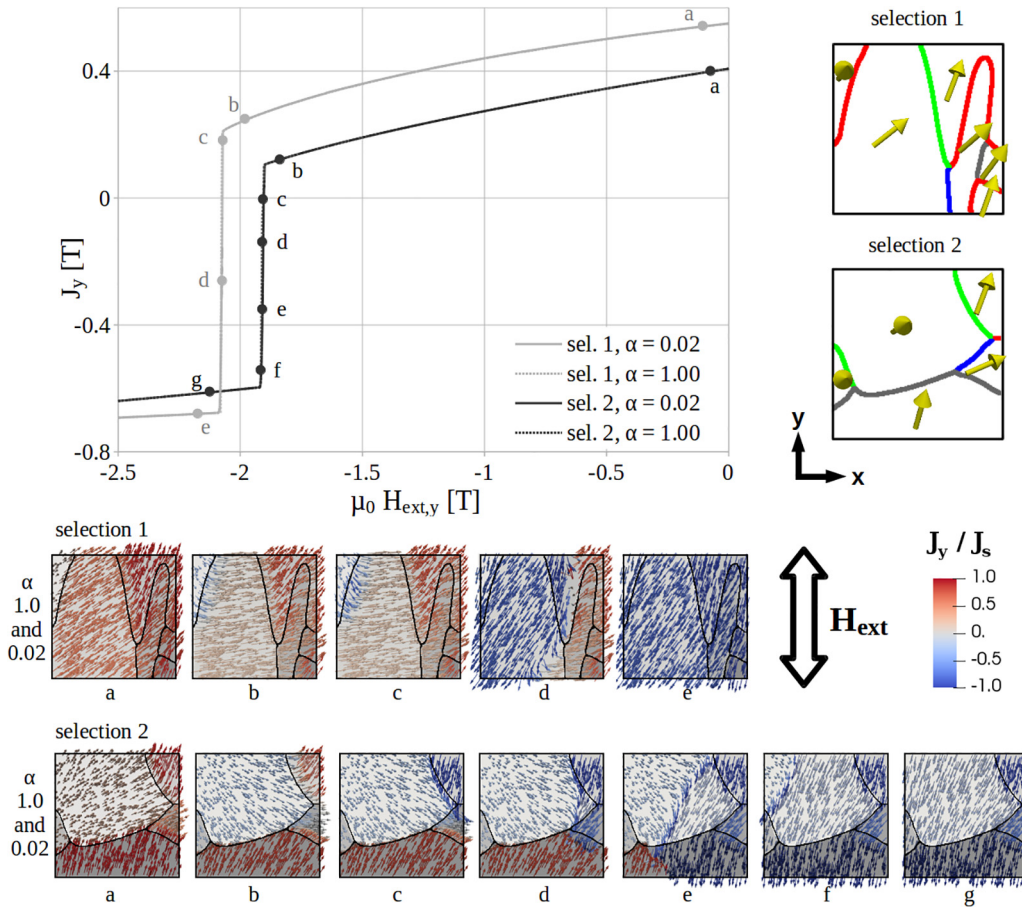


**Fig. 10.** Full demagnetization curves are computed for the selections 1 and 2 in Fig. 9 solving the LLG equations. Initial magnetization is set to 1 T in y direction. The hystereses are computed from an external field of 4 T to -4 T (shown only from 0 T to -2.5 T). Easy axes configurations are visualized with yellow arrows on the right. Twin boundaries: true-twins (red), order-fault-twins (green), pseudo-twins (blue), other boundaries (gray). Magnetic states are shown at the bottom with lower-case letters for Gilbert damping  $\alpha = 0.02$  and  $\alpha = 1.0$ . (For interpretation of the references to colour in this figure legend, the reader is referred to the web version of this article.)

Analyzing the demagnetization curves for the selections 1 and 2 in Fig. 9 show no difference, whether the Gilbert damping is set realistically to  $\alpha = 0.02$  or artificially to  $\alpha = 1.0$ . This is expected for low field rates [20,21]. During the demagnetization the domain wall is pinned at twin boundaries due to the local energy minima caused by the twinning angle  $\Theta$  (compare Fig. 7 and Fig. 8 with the simplified two grain model). This pinning event is shown in the magnetic states a and b of the selections. If the external field reaches a certain level, the energy barriers can be overcome, a spin wave originates and switches the rest of the material (c to e for selection 1 and c to g for selection 2).

### 3.5. Effect of Gilbert damping on the switching field

Even though it is expected that the Gilbert damping  $\alpha$  at low field rates has no effect on the switching field, it is not always true. Depending on the configurations of the twin boundaries, we observe that the smaller damping reduces the switching field. In other words an artificial damping of 1 leads to additional pinning at certain twin boundaries. In Fig. 11 we analyze the selections 3 and 4 of Fig. 9. We use the same simulation parameters as in the previous section.

The first pinning event can be followed at the magnetic states a and b for both selections and damping parameters. At c the first nucleation is occurring. For an artificial damping  $\alpha = 1.0$  a second pinning event happens (from c to d in both selections). Yet for a realistic damping of  $\alpha = 0.02$  no further pinning events can be observed and the whole sample reverses through expansion of the domain wall (c to g in selection 3 and c to f in selection 4). The switching field is drastically reduced with the low damping term. Interestingly the domain walls of the low and high damped simulations follow a different path during the switch. This could be related to the different paths the system follows according to the LLG equation solved for  $\alpha = 1.0$  and  $\alpha = 0.02$ . The

energy decay with time strongly depends on the Gilbert damping constant. For large  $\alpha$  the system follows a path that reduces the total energy quickly, whereas for small  $\alpha$  the system almost follows the contour line of the energy landscape [35,36]. Thus the system moves into a different region of the energy landscape while losing only a small amount of energy. Macroscopically this maybe seen in the different domain wall trajectories.

## 4. Summary and conclusion

We have demonstrated an automated toolchain for meshing microscopy data of MnAl-C grains. The EBSD data contains the crystallographic orientation. Using DREAM.3D or our own Python code, the data is transformed to a bitmap image with a coloring according to the crystallographic orientation. In several consecutive steps the bitmap image is vectorized to smooth the boundaries, increased in size and stored again as bitmap image. Some further image manipulation is necessary to obtain single colored orientation areas with smooth boundaries. A bottleneck in the image manipulation procedure is the vectorization of the pixelated bitmap. In this step each single color is vectorized and later on overlaid to a single image. Here certain problems can occur: boundaries of overlaying images do not coincide or small orientation areas could disappear. Changing the vectorizing algorithm could improve the stability of the automation process.

The enhanced bitmap image is prepared ideally for the inclusion into Iso2mesh. Here the 2D image is meshed with the Computational Geometry Algorithms Library (CGAL) into singular faces according to the color. In this work the very same layers are stacked to obtain a volumetric mesh. Alternatively several individual material slices could be used for the mesh generation. This procedure will be useful to simulate domain wall processes in thin samples observed by Lorentz



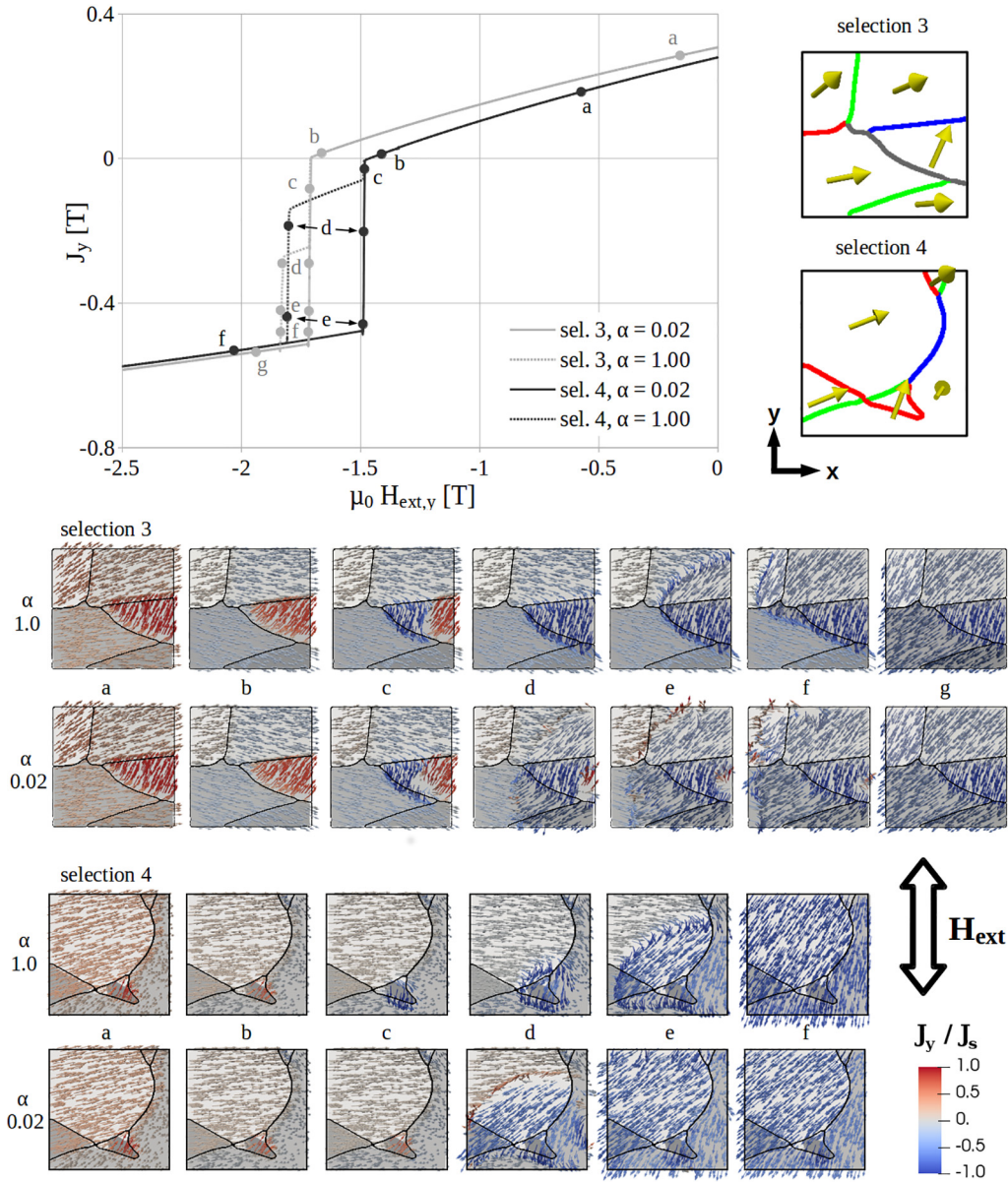


**Fig. 11.** Full demagnetization curves are computed for the selections 3 and 4 in Fig. 9 solving the LLG equations. Initial magnetization is set to 1 T in y direction. The hystereses are computed from an external field of 4 T to  $-4$  T (shown only from 0 T to  $-2.5$  T). Easy axes configurations are visualized with yellow arrows on the right. Twin boundaries: true-twins (red), order-fault-twins (green), pseudo-twins (blue), other boundaries (gray). Magnetic states are shown at the bottom with lower-case letters for Gilbert damping  $\alpha = 0.02$  and  $\alpha = 1.0$ . (For interpretation of the references to colour in this figure legend, the reader is referred to the web version of this article.)

transmission electron microscopy. In order to generate a three-dimensional model of the microstructure, that incorporates the magneto-static interaction field, the initially created volumetric mesh is transferred to the Salome package to add an airbox. This inclusion of the airbox, in its current implementation, has certain problems. Adding a graded mesh for the airbox to an existing mesh is error-prone. Dangling nodes and badly shaped elements should be avoided. It would be more feasible, in an advanced toolchain, to keep the meshing step within a single software package to reduce conversion errors.

We analyzed the influence of crystallographic defects using the time dependent Landau-Lifshitz-Gilbert equation. In this work we have chosen four selections of the native EBSD data to get an impression on the hysteresis properties. Results showed a widespread range of coercivity, which clearly indicates that twin boundaries greatly influence the hysteresis properties and thus the applicability as a permanent magnet. In order to improve the production routines for creating high

performance permanent magnets, a deeper understanding of the crystallographic defect is important. We investigated spin wave dynamics close to twinning junctions. Gilbert damping has a significant effect on the pinning behavior. An artificially introduced damping of 1, which is numerically preferable, introduces a second pinning event in some of our analyzed samples. The influence of the damping constant on the pinning fields are not unexpected and have been reported experimentally as for example in permalloy nanowires [37]. Here we could show, that realistically low damping in the simulations is reducing the switching field even for low field rates.

The automated meshing procedure in this work reduces time and effort for the model creation, enabling the production of huge simulation data for further analysis. The accuracy of the final mesh is certainly influenced by the quality of the initial dataset. Improving the EBSD measurements (increasing the information density) will have a positive effect. Important to notice is, that the automated EBSD meshing



procedure is not limited to micromagnetic simulations. There are many fields of research where finite element meshes are needed, which would benefit from the speed up in mesh generation from real material samples.

### Data availability

All data generated or analyzed during this study, including the created finite element meshes, are available from the corresponding author upon request.

### Acknowledgment

The authors gratefully acknowledge the financial support of the Austrian Science Fund (FWF), Project: I 3288-N36 and the German Research Foundation (DFG), Project: 326646134.

### References

- [1] H. Zijlstra, Coping with Brown's paradox: The pinning and nucleation of magnetic domain walls at antiphase boundaries, *IEEE Trans. Magn.* 15 (5) (1979) 1246–1250.
- [2] S. Bance, F. Bittner, T.G. Woodcock, L. Schultz, T. Schrefl, Role of twin and antiphase defects in MnAl permanent magnets, *Acta Mater.* 131 (2017) 48–56.
- [3] J. Jakubovics, T. Jolly, The effect of crystal defects on the domain structure of Mn-Al alloys, *Physica B+ C* 86 (1977) 1357–1359.
- [4] P. Nieves, S. Arapan, T. Schrefl, S. Cuesta-Lopez, Atomistic spin dynamics simulations of the MnAl  $\tau$ -phase and its antiphase boundary, *Phys. Rev. B* 96 (22) (2017) 224411.
- [5] J.V. Landuyt, G. Tendeloo, J. Broek, H. Donkersloot, H. Zijlstra, Defect structure and magnetic properties of MnAl permanent magnet materials, *IEEE Trans. Magn.* 14 (5) (1978) 679–681.
- [6] E. Houseman, J. Jakubovics, Electron microscope study of the domain structure of MnAlC magnets, *J. Magn. Magn. Mater.* 31 (1983) 1007–1008.
- [7] F. Bittner, L. Schultz, T.G. Woodcock, Twin-like defects in L10 ordered  $\tau$ -MnAl-C studied by EBSD, *Acta Mater.* 101 (2015) 48–54.
- [8] R. Quey, P. Dawson, F. Barbe, Large-scale 3D random polycrystals for the finite element method: Generation, meshing and remeshing, *Comput. Methods Appl. Mech. Eng.* 200 (17–20) (2011) 1729–1745.
- [9] J. Fischbacher, A. Kovacs, M. Gusenbauer, H. Oezelt, L. Exl, S. Bance, T. Schrefl, Micromagnetics of rare-earth efficient permanent magnets, *J. Phys. D: Appl. Phys.* 51 (19) (2018) 193002.
- [10] L. Exl, S. Bance, F. Reichel, T. Schrefl, H. Peter Stimming, N.J. Mauser, LaBonte's method revisited: an effective steepest descent method for micromagnetic energy minimization, *J. Appl. Phys.* 115 (17) (2014) 17D118.
- [11] J. Liu, H. Sepehri-Amin, T. Ohkubo, K. Hioki, A. Hattori, T. Schrefl, K. Hono, Grain size dependence of coercivity of hot-deformed Nd-Fe-B anisotropic magnets, *Acta Mater.* 82 (2015) 336–343.
- [12] O. Akdogan, H. Sepehri-Amin, N. Dempsey, T. Ohkubo, K. Hono, O. Gutfleisch, T. Schrefl, D. Givord, Preparation, characterization, and modeling of ultrahigh coercivity Sm-Co thin films, *Adv. Electron. Mater.* 1 (5) (2015) 1500009.
- [13] A.C. Reid, R.C. Lua, R.E. García, V.R. Coffman, S.A. Langer, Modelling microstructures with OOF2, *Int. J. Mater. Prod. Technol.* 35 (3–4) (2009) 361–373.
- [14] S. Ghosh, Y. Bhandari, M. Groeber, Cad-based reconstruction of 3d polycrystalline alloy microstructures from fib generated serial sections, *Comput. Aided Des.* 40 (3) (2008) 293–310.
- [15] P. Young, T. Beresford-West, S. Coward, B. Notarberardino, B. Walker, A. Abdul-Aziz, An efficient approach to converting three-dimensional image data into highly accurate computational models, *Philos. Trans. R. Soc. London A* 366 (1878) (2008) 3155–3173.
- [16] G. Legrain, P. Cartraud, I. Perreard, N. Moës, An x-fem and level set computational approach for image-based modelling: application to homogenization, *Int. J. Numer. Meth. Eng.* 86 (7) (2011) 915–934.
- [17] L. Madej, J. Wang, K. Perzynski, P.D. Hodgson, Numerical modeling of dual phase microstructure behavior under deformation conditions on the basis of digital material representation, *Comput. Mater. Sci.* 95 (2014) 651–662.
- [18] S. Dancette, A. Browet, G. Martin, M. Willemet, L. Delannay, Automatic processing of an orientation map into a finite element mesh that conforms to grain boundaries, *Modell. Simul. Mater. Sci. Eng.* 24 (5) (2016) 055014.
- [19] W. Scholz, D. Suess, T. Schrefl, J. Fidler, Micromagnetic simulation of structure–property relations in hard and soft magnets, *Comput. Mater. Sci.* 18 (1) (2000) 1–6.
- [20] T. Leineweber, H. Kronmüller, Dynamics of magnetisation states, *J. Magnet. Magn. Mater.* 192 (3) (1999) 575–590.
- [21] T. Leineweber, H. Kronmüller, Influence of the intrinsic dynamics of the magnetisation on the hysteresis loop, *Physica B* 275 (1–3) (2000) 5–10.
- [22] Q. Fang, D.A. Boas, Tetrahedral mesh generation from volumetric binary and grayscale images, in: *Biomedical Imaging: From Nano to Macro, 2009. ISBI'09. IEEE International Symposium on, Ieee, 2009*, pp. 1142–1145.
- [23] M. Humbert, N. Gey, J. Muller, C. Esling, Determination of a mean orientation from a cloud of orientations. application to electron back-scattering pattern measurements, *J. Appl. Crystallogr.* 29 (6) (1996) 662–666.
- [24] G. Nolze, R. Hielscher, Orientations—perfectly colored, *J. Appl. Crystallogr.* 49 (5) (2016) 1786–1802.
- [25] The CGAL Project, CGAL User and Reference Manual, 4.11.1 Edition, CGAL Editorial Board, 2018. <http://doc.cgal.org/4.11.1/Manual/packages.html>.
- [26] J. Ahrens, B. Geveci, C. Law, C. Hansen, C. Johnson, Paraview: An end-user tool for large-data visualization, *The visualization handbook* 717.
- [27] Q. Chen, A. Konrad, A review of finite element open boundary techniques for static and quasi-static electromagnetic field problems, *IEEE Trans. Magn.* 33 (1) (1997) 663–676.
- [28] J. Fidler, T. Schrefl, Micromagnetic modelling-the current state of the art, *J. Phys. D: Appl. Phys.* 33 (15) (2000) R135.
- [29] D. Suess, V. Tsiantos, T. Schrefl, J. Fidler, W. Scholz, H. Forster, R. Dittrich, J. Miles, Time resolved micromagnetics using a preconditioned time integration method, *J. Magn. Magn. Mater.* 248 (2) (2002) 298–311.
- [30] J. Thielsch, F. Bittner, T.G. Woodcock, Magnetization reversal processes in hot-extruded MnAl-C, *J. Magn. Magn. Mater.* 426 (2017) 25–31.
- [31] E.C. Stoner, E. Wohlfarth, A mechanism of magnetic hysteresis in heterogeneous alloys, *Phil. Trans. R. Soc. Lond. A* 240 (826) (1948) 599–642.
- [32] R. Yilgin, M. Oogane, S. Yakata, Y. Ando, T. Miyazaki, Investigation on intrinsic gilbert damping constant in co/sub 2/mnal heusler alloy films, *Magnetics Conference, 2005. INTERMAG Asia 2005. Digests of the IEEE International, IEEE, 2005*, pp. 1871–1872.
- [33] S. Mizukami, Y. Ando, T. Miyazaki, The study on ferromagnetic resonance line-width for nm/80nm/nm (nm = cu, ta, pd and pt) films, *Jpn. J. Appl. Phys.* 40 (2R) (2001) 580.
- [34] R. Kikuchi, On the minimum of magnetization reversal time, *J. Appl. Phys.* 27 (11) (1956) 1352–1357.
- [35] D. Suess, T. Schrefl, J. Fidler, Reversal modes, thermal stability and exchange length in perpendicular recording media, *IEEE Trans. Magn.* 37 (4) (2001) 1664–1666.
- [36] D. Suess, T. Schrefl, W. Scholz, J. Fidler, Fast switching of small magnetic particles, *J. Magn. Magn. Mater.* 242 (2002) 426–429.
- [37] T.A. Moore, P. Möhrke, L. Heyne, A. Kaldun, M. Kläui, D. Backes, J. Rhensius, L.J. Heyderman, J.-U. Thiele, G. Woltersdorf, et al., Magnetic-field-induced domain-wall motion in permalloy nanowires with modified gilbert damping, *Phys. Rev. B* 82 (9) (2010) 094445.